Action Observation With Rhythm Imagery (AORI): A Novel Paradigm to Activate Motor-Related Pattern for High-Performance Motor Decoding

Yuxuan Wei, Jianjun Meng, *Senior Member, IEEE*, Ruijie Luo, Ximing Mai, Songwei Li, Yuchen Xia, and Xiangyang Zhu

Abstract*—*Objective: **The Motor Imagery (MI) paradigm has been widely used in brain-computer interface (BCI) for device control and motor rehabilitation. However, the MI paradigm faces challenges such as comprehension difficulty and limited decoding accuracy. Therefore, we propose the Action Observation with Rhythm Imagery (AORI) as a natural paradigm to provide distinct features for high-performance decoding.** ***Methods:*** **Twenty subjects were recruited in the current study to perform the AORI task. Spectral-spatial, temporal and time-frequency analyses were conducted to investigate the AORI-activated brain pattern. Task-discriminant component analysis (TDCA) was utilized to perform multiclass motor decoding.** ***Results:*** **The results demonstrated distinct lateralized ERD in the alpha and beta bands, and clear lateralized steady-state movement-related rhythm (SSMRR) at the movement frequencies and their first harmonics. The activated brain areas included frontal, sensorimotor, posterior parietal, and occipital regions. Notably, the decoding accuracy reached 92.16% $\pm$ 7.61% in the four-class scenario.** ***Conclusion and Significance:*** **We proposed the AORI paradigm, revealed the activated motor-related pattern and proved its efficacy for high-performance motor decoding. These findings provide new possibilities for designing a natural and robust BCI for motor control and motor rehabilitation.**

***Index Terms*—Action observation (AO), brain-computer interface (BCI), electroencephalogram (EEG), motor imagery (MI), steady-state movement-related rhythm (SSMRR).**

I. Introduction

THE brain-computer interface (BCI) provides a novel method for establishing a connection between the brain and the external environment [1], [2]. Motor Imagery (MI) is an important paradigm for BCI, as it enables the translation of subjective motor intentions into corresponding commands and holds significant potential in reconstructing or restoring motor control pathways [3], [4]. Although MI-BCI has achieved considerable advancement in device control [5], [6], [7] and motor rehabilitation [8], [9], it still encounters well-acknowledged challenges. Firstly, MI is an abstract mental task, which leads to difficulties for subjects in comprehending and performing it [10], [11], [12]. Moreover, MI-BCI often faces low decoding accuracy and even MI-inefficiency [13], [14].

Researchers have introduced Action Observation (AO) and AO-guided MI to overcome the abstract nature of MI. Compelling evidence has demonstrated that AO and MI can elicit similar activities in the motor system, this phenomenon is particularly manifested in the modulation of the sensorimotor rhythm (SMR) [11], [15]. In clinical practice for motor rehabilitation, AO and MI have independently been validated as effective paradigms [16], [17], [18]. Furthermore, many studies have employed a combination of AO and MI (AO-guided MI) [19], [20], [21]. On the one hand, the integration of AO and MI enables subjects to develop a more intuitive perception of imagined movements, thereby rendering the tasks more concrete. On the other hand, the utilization of AO-guided MI may augment corresponding physiological features such as event-related desynchronization (ERD), consequently enhancing motor decoding performance and facilitating motor recovery.

The introduction of AO, however, remains insufficient in enhancing the decoding accuracy to a satisfactory level [22], primarily because a considerable portion of subjects exhibit weak ERD features resulting from their limited ability to modulate SMR effectively. Recently, researchers have been dedicated to further advancing the AO-guided MI paradigm, aiming to employ more available physiological features beyond ERD. One approach is to combine AO-guided MI with steady-state visual evoked potential (SSVEP) [23], [24]. In the study [24], the paradigm was designed as follows: action images of

Received 17 June 2024; revised 3 September 2024; accepted 24 October 2024. Date of publication 28 October 2024; date of current version 21 February 2025. This work was supported by the National Natural Science Foundation of China under Grant 52175023. *(Yuxuan Wei and Jianjun Meng are co-first authors.) (Corresponding authors: Jianjun Meng; Xiangyang Zhu.)*

Yuxuan Wei, Ruijie Luo, Ximing Mai, Songwei Li, and Yuchen Xia are with the School of Mechanical Engineering, Shanghai Jiao Tong University, China, and also with the State Key Laboratory of Mechanical System and Vibration, Shanghai Jiao Tong University, China.

Jianjun Meng and Xiangyang Zhu are with the School of Mechanical Engineering, Shanghai Jiao Tong University 200240, China, and also with the State Key Laboratory of Mechanical System and Vibration, Shanghai Jiao Tong University 200240, China (e-mail: mengjianjunxs008@sjtu.edu.cn; mexyzhu@sjtu.edu.cn).

This article has supplementary downloadable material available at https://doi.org/10.1109/TBME.2024.3487133, provided by the authors.

Digital Object Identifier 10.1109/TBME.2024.3487133

ball-gripping were presented successively on the screen while flickering at specific stimulus frequencies. Participants were instructed to focus on the designated target for the SSVEP task while simultaneously performing the MI task by mimicking the gripping action. With this paradigm, the accuracy of left-right binary classification for participants increased from approximately 80% (using MI-induced features alone) to 95%. Although the introduction of SSVEP significantly improved decoding accuracy, it also raised concerns about inducing visual fatigue and discomfort [25]. Another group of researchers has developed a new paradigm based on steady-state motion visual evoked potential (SSMVEP) [14], [22], [25], [26], [27], [28], which can reduce visual fatigue and discomfort [14], [27], [29]. Different from the stimulus in the hybrid paradigm of SSVEP and MI, the stimulus of SSMVEP is precisely designed using the frame rate reduction (FRR) method [22], [28]. Each SSMVEP stimulus contains a pair of frame rate and movement frequency (for example, 7.5 Hz and 0.8333 Hz) [28]. Results have demonstrated that SSMVEP paradigm can simultaneously induce responses at the frame rate (and its harmonics) in the occipital region and ERD in the sensorimotor region [14], [22], [28]. The primary limitation of the SSMVEP paradigm derives from its relatively complex stimulus design. Additionally, the design involves calculations directly related to the screen's refresh rate, thereby diminishing the universality of the paradigm.

Our previous study has shown that movement frequency can be decoded from the electroencephalogram (EEG) using the steady-state movement-related rhythm (SSMRR) [30]. In contrast to the high-frequency (above 6 Hz) SSVEP and SSMVEP induced by exogenous stimulus, SSMRR is a low-frequency (1-3 Hz) steady-state rhythm induced by voluntary rhythmic movement. Since SSMRR provides informative features encompassing movement frequency, it may serve as a physiological basis for designing novel paradigms. Specifically, an AO-guided rhythmic MI paradigm can be designed. This paradigm eliminates the need for high-frequency stimulus and simplifies the paradigm design by solely utilizing videos of movements with different frequencies as the visual guide.

The AO-guided rhythmic MI paradigm presents us with three primary challenges. Firstly, accurately performing rhythmic MI at a fixed frequency is not trivial. While AO reduces the task abstraction and provides a guide of movement frequency, concurrently performing AO and a complex rhythmic MI task can lead to increased cognitive load. Considering that AO has already facilitated the construction of the movement scenario, subjects can be relieved from the cognitive burden of mentally creating a bodily movement scene [11]. That means the mental task can be simplified to rhythm imagery from rhythmic movement imagery. Therefore, we propose the Action Observation with Rhythm Imagery (AORI) paradigm. In this paradigm, subjects voluntarily engage in rhythm imagination guided by the video, while AO provides a sense of agency [31], [32]. The second challenge lies in the unknown brain pattern activated by AORI. Inspired by the finding that rhythmic movement can induce SSMRR, which encodes movement frequency [30], we expect that the AORI paradigm can also induce similar electrophysiological characteristics. However, previous non-invasive researches on movement frequency encoding have predominantly focused on real movements [33], [34], [35]. To our knowledge, only one early study has involved motor imagery, but it did not involve action observation [36]. In the current study, we aim to explore the motor-related pattern activated by the AORI paradigm from multiple perspectives, including spectral-spatial, temporal, and time-frequency domains. The third challenge is to employ a proper decoding algorithm to efficiently utilize the features induced by AORI paradigm. In the conventional MI paradigm, the utilized feature is SMR, and the benchmark decoding framework is FBCSP-SVM/LDA (FBCSP refers to filter-bank common spatial pattern, SVM refers to support vector machine, and LDA refers to linear discriminant analysis) [37], [38], [39]. Nevertheless, FBCSP and its derivative methods were not designed to process the periodic feature (such as SSMRR) that encodes frequency. Motivated by SSVEP decoding, we anticipated that the state-of-the-art algorithms for processing periodic features such as task-discriminant component analysis (TDCA) [40] and task-related component analysis (TRCA) [41] could be effective for the AORI paradigm. In the present study, we employed TDCA due to its superior performance compared to TRCA in previous SSVEP studies. In summary, this study contributes in the following aspects: (1) Introduced a novel BCI paradigm named AORI, which is easily understandable and design-friendly; (2) Conducted a comprehensive investigation into the brain patterns activated by the AORI; (3) Validated that high-performance motor decoding (over 90% accuracy for 4-class decoding) can be achieved based on AORI paradigm.

II. Methods

A. Participants

Twenty-three healthy subjects (aged 19–27, six female) were randomly recruited from the campus. All participants had normal or corrected-to-normal vision. No history of neurological disorders was reported. Informed consent was obtained from all participants prior to the experiment, and participants received monetary compensation upon completion. This study was approved by the Institutional Review Board of Shanghai Jiao Tong University (IRB HRP E2021216I).

EEG data from three subjects were excluded from formal analysis due to irreversible contamination. Among the 20 subjects included in the formal analysis, three (S1, S2, S17) had prior experience with traditional motor imagery experiments, while the others had no previous BCI experiences.

B. Paradigm Design and Experimental Setup

The core of AORI involves focusing attention on the moving hand in the video while imagining a rhythm guided by the viewed movement. The pre-recorded video depicts two hands, with either the left or right hand rhythmically moving up and down at a fixed frequency (supplementary video 1-4). Before the experiment, we gave participants the following instructions on how to perform the AORI:

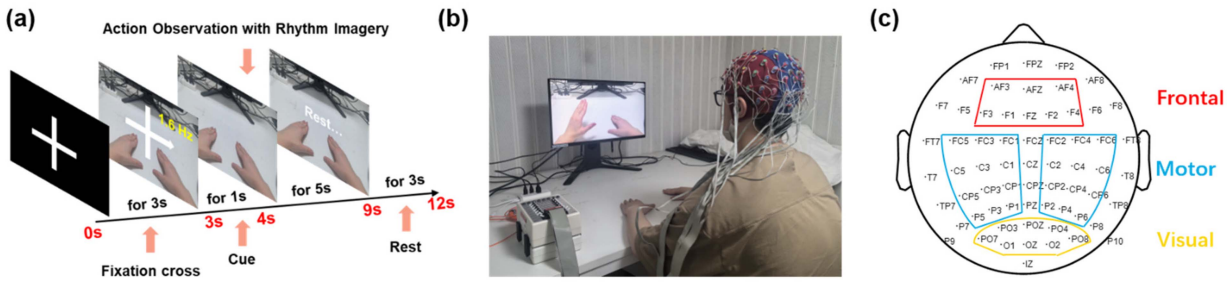

Fig. 1. (a) The time sequence of a trial. (b) The experimental setup. (c) Electrode placement and the three regions we evaluated for the decoding.

1) Among the two hands displayed on the screen, they needed to concentrate on the hand in motion.
2) Imagine the rhythm of the movement, ensuring it aligns with the motion rhythm in the video. This is similar to maintaining a covert beat inherently, but we instructed participants to imagine the continuous undulation of the movement, rather than imagine a discrete beat.
3) The third point serves as a prompt rather than a task requirement. We informed participants that if they experienced a sensation as though their own hand was moving or if they perceived an illusion of driving the hand on the screen, it would indicate a full understanding and correct conduction of the AORI. However, the absence of such sensations does not necessarily imply incorrect performance.
4) Although we did not require participants to imagine a clear concept of hand movement, if a participant felt there was little difference between imagining rhythmic hand movements and imagining rhythms, they could also directly perform rhythmic movement imagery.

In the current study, the experiment comprises four classes of tasks: 1 Hz-left hand, 1.2 Hz-right hand, 1.4 Hz-left hand, and 1.6 Hz-right hand. The time sequence of a trial is shown in Fig. 1(a): At t = 0 s, a white fixation cross appears on the screen for 3 seconds. Subsequently, the task cue is presented for 1 second, indicating either a left-hand or right-hand arrow along with the task frequency. Following this, the 4 s–9 s constitutes the AORI stage, during which participants perform the aforementioned AORI task. Finally, there is a 3-second rest period. The experiment includes a total of 6 runs. Each run consists of 40 trials (with 10 trials per task type, block-randomized), and the inter-trial interval is 1 second. Prior to the formal experiment, each participant practiced AORI for about 3 minutes and verbally confirmed comprehension of this task.

During the experiment, participants were seated in a comfortable chair in an electromagnetically shielded, noise-free room (Fig. 1(b)). The experiment was conducted using the BCI2000 platform [42].

C. Data Acquisition and Preprocessing

EEG data were acquired by a 64-channel Biosemi Active Two system (Biosemi, Amsterdam, The Netherlands) at a sampling rate of 1024 Hz. Each subject was fitted with a properly sized cap with active electrodes in the international 10-20 manner. The electrode offsets were carefully maintained within the range of ±20 mV.

The preprocessing was performed using MATLAB R2022a (MathWorks, USA) with EEGLAB toolbox [43]. Raw EEG data were 0.7-40 Hz bandpass filtered, common average referenced, and then down-sampled to 256 Hz. Artifact subspace reconstruction (ASR) was used to mitigate artifacts [44]. The cutoff parameter was set to 20 based on the literature. Subsequently, ocular and muscle artifacts were further eliminated after independent component analysis (ICA).

An epoch was selected as −0.5 s to 12 s relative to the 0 s of each trial. Therefore, each subject has a total of 240 EEG epochs (60 epochs per task type) for further analysis. The size of the epoch is 64 × 3200, where 64 is the number of channels, and 3200 is the number of time points (256 × 12.5, sampling rate × time length).

D. Electrophysiological Analysis

1) Spectral-Spatial Analysis: We utilized coherence analysis to investigate the spectral and spatial pattern corresponding to the movement frequency. Coherence is a commonly used metric for assessing the coupling of two time series at a specific frequency. For each kind of task, we created a reference signal that contains the movement frequency and its harmonics as follows:

$$y\left(t\right)=\sum_{m=1}^{4}\sin\left(2\pi\left(m\times f_{move}\right)t\right)+0.2\times n\left(t\right) \quad (1)$$

where f_{move} is the movement frequency of the task, and $n(t)$ is the white noise. We computed the coherence between the signal from each channel and the reference signal to reveal the spectral-spatial distribution of the EEG component at the movement frequency and its harmonics. Specifically, the coherence was calculated using formula (2):

$$Coh_{xy}\ \left(f\right)=\frac{\left|\sum_{i=1}^{N}X_i\left(f\right)Y_i^*\left(f\right)\right|^2}{\sum_{i=1}^{N}\left|X_i\left(f\right)\right|^2\sum_{i=1}^{N}\left|Y_i\left(f\right)\right|^2} \quad (2)$$

where $X_i(f)$ and $Y_i(f)$ denote the Fourier transforms of the i th segments of EEG signals x and reference signal y at the

frequency f, and the symbol '$*$' denotes the complex conjugate. In our study, the number of segments is 60 ($N = 60$) since we conducted 60 trials for each type of task. A segment of EEG signal x represents the 4 s–9 s of a trial, while a segment of reference signal y represents 5-second data generated using formula (1). The range of t for each segment of y needs to be consistent.

We also investigated the spatial patterns of ERD in alpha and beta bands (sensorimotor rhythms) during the AORI. In particular, we calculated each channel's power change during the AORI stage (4 s–9 s) compared to the baseline (0 s–2 s) by formula (3) and (4):

$$alphaERD = 10\log_{10}\frac{mean(PSD_{AORI}\,(alphaband))}{mean(PSD_{baseline}\,(alphaband))} \tag{3}$$

$$betaERD = 10\log_{10}\frac{mean(PSD_{AORI}\,(betaband))}{mean(PSD_{baseline}\,(betaband))} \tag{4}$$

The alpha and beta bands were selected as 8–13 Hz and 16-30 Hz, respectively. The power spectral density (PSD) was computed using a 0.5 s-length Hann window with a 50% overlap.

2) Temporal Analysis: In the time domain, we mainly focused on the waveform after the grand average. For each type of task, all 60 trials from all 20 subjects were grand-averaged. The EEG data were further 0.5–5 Hz bandpass filtered using a 4th-order Butterworth filter before the grand average to highlight the frequency band of interest.

3) Time-Frequency Analysis: In the time-frequency domain, we calculated event-related spectral perturbation (ERSP) to assess the power changes and inter-trial phase clustering (ITPC) to assess the phase-locking. The calculation formula of ERSP for N trials is defined as follows:

$$ERSP\ (f,t) = \frac{1}{N}\sum_{k\,=\,1}^{N} F_k(f,t)^2 \tag{5}$$

where $F_k(f,t)$ denotes the spectral estimation of the kth trial at frequency f and time t. The *newtimef* function in EEGLAB was employed to compute the ERSP from 0.8 Hz to 35 Hz, and the "wavelet cycles" parameter was set to [3, 0.8]. The baseline was set as 2 s–3 s of the trial.

The time-frequency ITPC was calculated using formula (6):

$$ITPC\ (f,t) = \left|\frac{1}{N}\sum_{k=1}^{N} e^{i\theta_k(t,f)}\right| \tag{6}$$

where N is the number of trials, and $\theta_k(t,f)$ represents the phase angle of the kth trial at frequency f and time t.

E. Decoding Methods

1) SSMRR-Based Decoding: TDCA was utilized to perform the SSMRR-based motor decoding under the AORI paradigm since it is the state-of-the-art method to process rhythmic signals. TDCA is a data-driven method that applies a trained spatial filter to the input data, and subsequently accomplishes multiclass decoding through template matching.

The preliminary stage of TDCA is a two-step data augmentation. In the following part, the data from a trial will be represented by $\boldsymbol{X} \in \mathbb{R}^{N_c \times N_t}$, where N_c represents the number of channels and N_t represents the number of time points. The step one of augmentation is:

$$\tilde{\boldsymbol{X}} = \left[\boldsymbol{X}^T, \boldsymbol{X}_1^T, \ldots, \boldsymbol{X}_l^T\right]^T \tag{7}$$

where $\tilde{\boldsymbol{X}} \in \mathbb{R}^{(l+1)N_c \times N_t}$ is the augmented data of $\boldsymbol{X}$, and $\boldsymbol{X}_l \in \mathbb{R}^{N_C \times N_t}$ is obtained by delaying l time points for $\boldsymbol{X}$. Next, the step two of augmentation is:

$$\boldsymbol{X}_a = \left[\tilde{\boldsymbol{X}}, \tilde{\boldsymbol{X}}_p\right] \tag{8}$$

where $\boldsymbol{X}_a \in \mathbb{R}^{(l+1)N_c \times 2N_t}$ is the augmented data of $\tilde{\boldsymbol{X}}$, and $\tilde{\boldsymbol{X}}_p$ is the projection of $\tilde{\boldsymbol{X}}$ in the orthogonal space defined by sine-cosine reference signals [40]. In this study, the frequencies of sine-cosine references are the movement frequencies and their first harmonics.

The core of TDCA involves the utilization of a two-dimensional linear discriminant analysis (LDA) to optimize a spatial filter, aiming to maximize the between-class difference while minimizing the within-class difference. The between-class difference matrix $\boldsymbol{H}_b \in \mathbb{R}^{(l+1)N_c \times 2N_{class}N_t}$ and the within-class difference matrix $\boldsymbol{H}_w \in \mathbb{R}^{(l+1)N_c \times 2N_{trial}N_t}$ are formed as:

$$\boldsymbol{H}_b = \frac{1}{\sqrt{N_{class}}}\left[\bar{\boldsymbol{X}}_a^1 - \bar{\boldsymbol{X}}_a^a, \ldots, \bar{\boldsymbol{X}}_a^{N_{class}} - \bar{\boldsymbol{X}}_a^a\right] \tag{9}$$

$$\boldsymbol{H}_w = \frac{1}{\sqrt{N_{trial}}}\left[\boldsymbol{X}_a^{(1)} - \bar{\boldsymbol{X}}_a^{(1)}, \ldots, \boldsymbol{X}_a^{(N_{trial})} - \bar{\boldsymbol{X}}_a^{(N_{trial})}\right] \tag{10}$$

where N_{trial} is the number of the training trials from all classes and N_{class} is the number of classes. $\boldsymbol{X}_a^{(i)}$ is the data from ith trial, and $\bar{\boldsymbol{X}}_a^{(i)}$ is the mean of the class corresponding to the ith trial. $\bar{\boldsymbol{X}}_a^k$ is the mean of kth class, and $\bar{\boldsymbol{X}}_a^a$ is the mean of all trials. The spatial filter $\boldsymbol{W} \in \mathbb{R}^{(l+1)N_c \times (l+1)N_c}$ is obtained by solving the following optimization:

$$\hat{\boldsymbol{W}} = \underset{\boldsymbol{W}}{argmax}\ \frac{tr\left(\boldsymbol{W}\boldsymbol{H}_b{\boldsymbol{H}_b}^T\boldsymbol{W}^T\right)}{tr\left(\boldsymbol{W}\boldsymbol{H}_w{\boldsymbol{H}_w}^T\boldsymbol{W}^T\right)} \tag{11}$$

Usually, $\tilde{\boldsymbol{W}} \in \mathbb{R}^{(l+1)N_c \times N_{sub}}$, the first N_{sub} subspaces of $\hat{\boldsymbol{W}}$, will be used.

In the testing stage, the testing data will undergo the same augmentation. Then the label $\hat{k}$ is predicted by:

$$\begin{aligned} \rho_k &= corrcoef\left(\left(\boldsymbol{X}_a^k\right)^T\tilde{\boldsymbol{W}},\ \left(\bar{\boldsymbol{X}}_a^k\right)^T\tilde{\boldsymbol{W}}\right), \\ & k \in \{1, \ldots, N_{class}\} \\ \hat{k} &= \underset{k}{argmax}\ \rho_k \end{aligned} \tag{12}$$

where the function *corrcoef* conducts the two-dimensional correlation analysis and $\boldsymbol{X}_a^k$ represents the augmented testing sample with respect to the kth class. The two aforementioned hyperparameters, the number of delays l and the number of subspaces N_{sub} were set as 1 and 10.

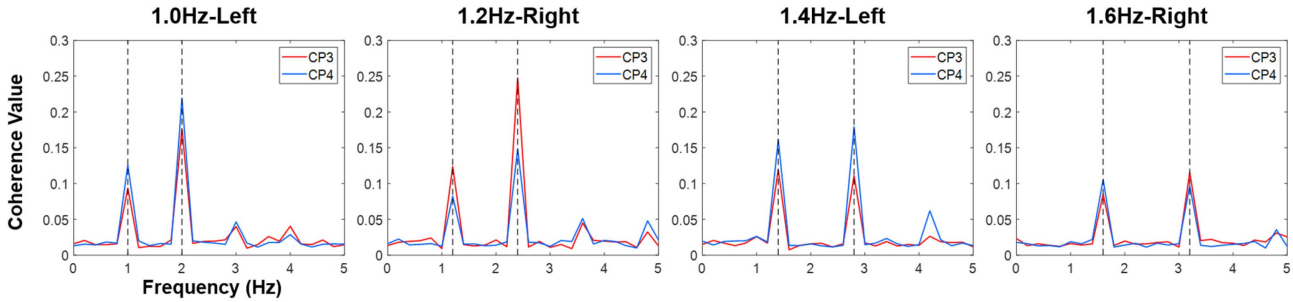

Fig. 2. The group-level coherence spectra for each type of task. CP3 and CP4 were presented as the representative channel here. The movement frequencies and their first harmonics were marked with black dashed lines.

2) SMR-Based Decoding: We also evaluated the performance of the SMR-based binary decoding, as the AORI paradigm may also elicit lateralized ERD in the sensorimotor rhythm. Here, we did not discriminate the movement frequency of the task, but used all of the trials and only divided all trials into two categories based on the left and right labels.

The filter-bank common spatial pattern (FBCSP) and support vector machine (SVM) were employed for feature extraction and classification, respectively. The range for selecting the filter-bank was 8–32 Hz, with a bandwidth of 4 Hz and a 50% overlap.

3) Channel Selection and Cross-Validation: The evaluation of decoding performance involved channels from three distinct regions: frontal, motor, and visual regions (Fig. 1(c)). The motor channels were from the supplementary motor area (SMA), premotor area (PMA), primary sensorimotor region (SM1), and posterior parietal cortex (PPC). The visual channels were from the occipital lobe, as well as the junction area between the occipital lobe and parietal lobe.

For the SSMRR-based decoding, we evaluated the decoding performance achieved using individual regions as well as combinations of regions. For SMR-based decoding, we only assessed the motor region's decoding performance.

The 10×4-fold cross-validation was utilized in this study. This process included randomly dividing all trials into four sets for the purpose of 4-fold cross-validation, and repeating this procedure ten times. Additionally, it should be noted that we only used the AORI stage (4 s–9 s) data from each trial for decoding.

F. Statistical Analysis

A statistical threshold of coherence is estimated using formula (13) [45]:

$$Coh_{threshold} = 1 - p^{\frac{1}{N-1}} \tag{13}$$

where p represents the p-value and N represents the number of disjoint segments used for calculating coherence. Specifically, we utilized $p = 0.05$ and N is equal to the number of used trials ($N = 60$). For each channel, its corresponding coherence can be compared with the significant threshold. Considering multiple comparisons correction, the p-value was adjusted using the Bonferroni correction based on the number of channels (n = 64).

The Wilcoxon signed-rank test was employed to compare decoding results pairwise using different channels.

III. Results

A. Spectral-Spatial Pattern

The group-level coherence spectra are illustrated in Fig. 2. Here, we selected CP3 and CP4 as the representative channels. Coherence spectra peaks were observed at the movement frequencies and their first harmonics. Peaks at higher-order harmonics were much weaker. In the left-hand AORI task, peaks at CP4 were higher than those at CP3, whereas in the right-hand AORI task, the opposite pattern was observed, indicating the presence of lateralization.

Furthermore, we utilized the form of topology to directly demonstrate the spatial pattern of the EEG activity coupling with movement frequency and its first harmonic. For each of the 64 channels, we counted the number of subjects whose coherence values exceeded the significant threshold, and used it as the channel's value. Specifically, these values were normalized by the total number of subjects (n = 20). A value of '1' signifies that all subjects exhibited significant coherence in that channel. Consequently, this topology (Fig. 3(a)) reflects the group-level spatial distribution of SSMRR induced by the AORI. In different types of tasks, the spatial distribution of SSMRR exhibited relatively consistent patterns. At the fundamental frequency, SSMRR was predominantly distributed in the central and occipital regions, extending to a broader range, including the frontal, sensorimotor, and posterior parietal regions. In the occipital and posterior parietal regions, SSMRR was more pronounced on the contralateral side of the task hand, while there was no obvious lateralization in the frontal and central regions. At the first harmonic of the movement frequency, the spatial distribution of SSMRR differed from that at the fundamental frequency. The distribution of SSMRR was primarily observed in the posterior parietal and occipital regions, exhibiting a distinct lateralization in the posterior parietal region while lacking it in the occipital region.

The spatial patterns of ERD in alpha and beta bands are presented in Fig. 3(b). In the alpha band, clear ERD was observed in the prefrontal, sensorimotor, and posterior parietal regions. Lateralized ERD was observed specifically in sensorimotor and

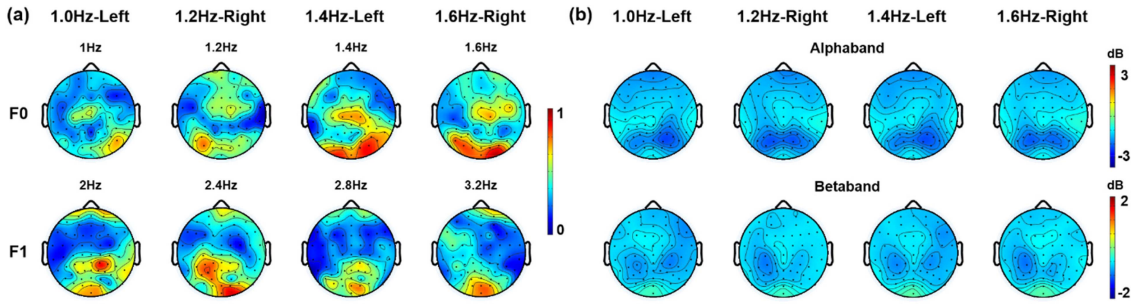

Fig. 3. (a) Group-level spatial pattern of SSMRR at the movement frequencies and their first harmonics. For each of the 64 channels, the number of subjects whose coherence exceeded the significant threshold ($p < 0.05$, Bonferroni corrected) was used as the channel's value. The value was normalized by the number of subjects ($n = 20$). (b) Group-level spatial pattern of ERD in alpha and beta bands.

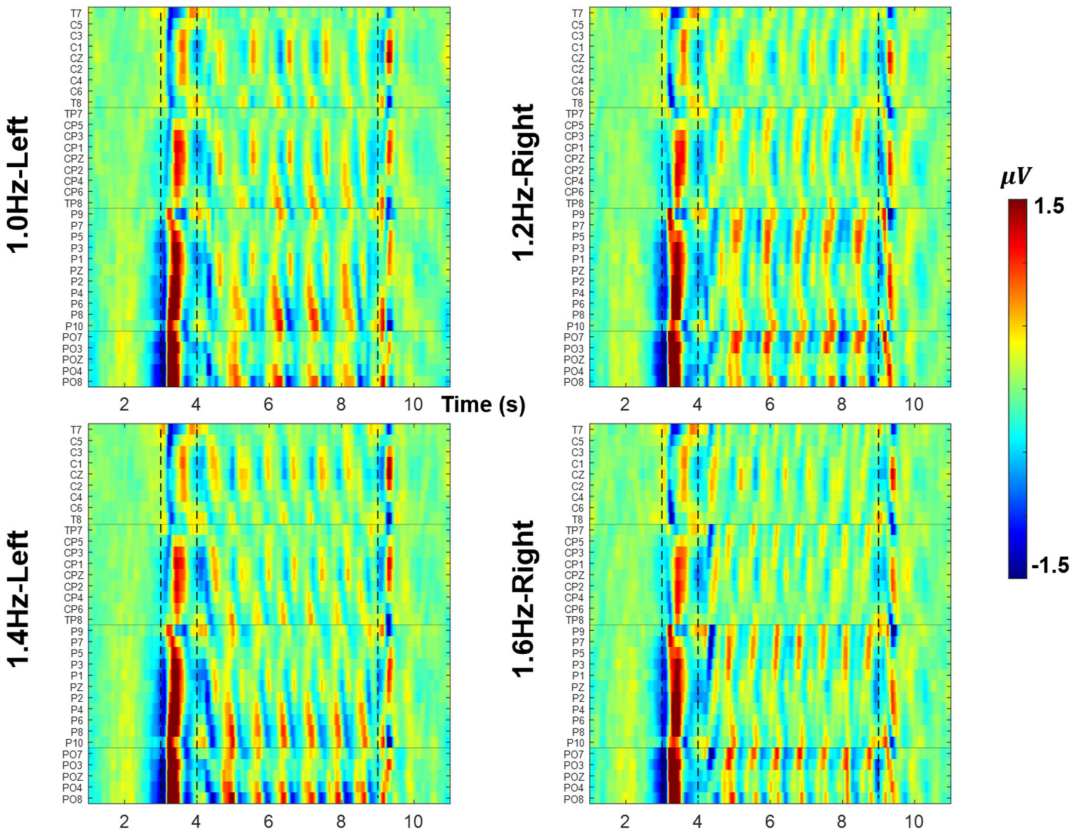

Fig. 4. Grand-averaged EEG time series. The x-axis represents time, the y-axis represents channels, and the color depicts amplitude. Rows of channels on the EEG cap were separated by horizontal lines. The appearance of the task cue and the start and end of the AORI stage were marked with dashed vertical lines.

posterior parietal regions, with the most pronounced ERD occurring in the latter. In the beta band, ERD was mainly distributed in the sensorimotor region and extended to the junction between the sensorimotor and posterior parietal regions. Additionally, a lateralization can also be observed. The ERD in the beta band was overall weaker than that in the alpha band.

B. Temporal Characteristics

We presented the grand-averaged EEG time series as 2D plots (Fig. 4), with the x-axis representing time, the y-axis representing channels, and the amplitude depicted by color. To enhance the clarity of the graph, we divided each row of channels on the EEG cap into subregions, which were separated by horizontal lines in the figure. The appearance of the task cue and the start and end of the AORI stage were marked with dashed vertical lines in the figure. The figure, which contains all 64 channels, can be found in supplementary Fig. 1.

Firstly, clear periodic activities consistent with the corresponding movement frequency can be observed in different tasks. Secondly, lateralization was demonstrated and can be directly reflected in the amplitudes of channels from parietal and occipital regions (e.g., CPx, Px, POx). Moreover, phase differences were observed among different channels, with the

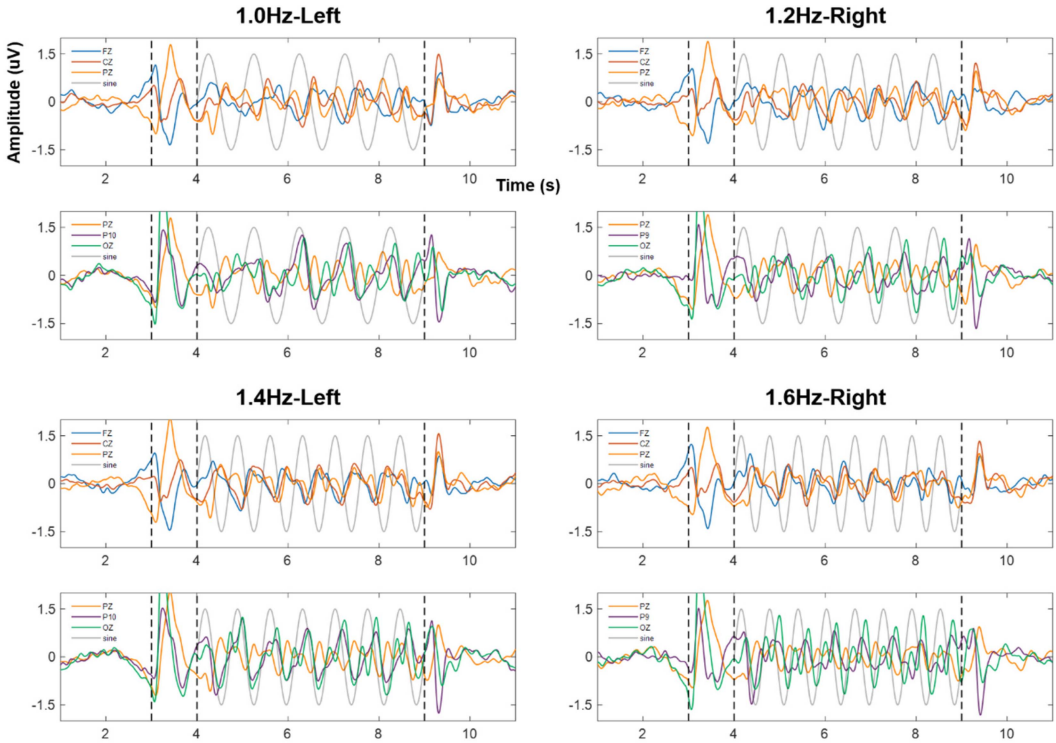

Fig. 5. Grand-averaged EEG time series from several representative channels. For each type of task, we selected five channels: four along the midline and one in the parietal region on the contralateral side of the task-related hand. To present the results more clearly, the five channels were plotted in two separate subplots, with the Pz channel appearing in both plots. Sine waves at the movement frequencies were given as references (the grey curves), which could be regarded as the speed curves of the observed hand movements. These results directly illustrated the similarities and differences in temporal characteristics and phases across different channels.

parietal region exhibiting the most pronounced phenomenon. Specifically, within a subregion, centrally located channels demonstrated leading phases compared to those on both sides (e.g., Pz in comparison to P9 and P10).

We selected several representative channels to further illustrate the waveform and phase characteristics of the time series, as shown in Fig. 5 (The time series of all 64 channels can be found in Supplementary Figs. 2, 3, 4, and 5). Sine waves at the movement frequencies were given as references. The sine wave could be regarded as the speed curve of the observed hand movement. From the waveform, it is evident that Pz and Oz indicated a distinct first harmonic besides the activity at the fundamental frequency. In terms of phase, the phases of Fz, Cz, and Pz were generally consistent, lagging behind the sine wave by approximately half a cycle (Note: When discussing phase, we do not consider harmonics). Oz and P9/P10 were generally in phase with the sine wave and lagged behind Pz. Additionally, we observed that Oz and P9/P10 reached a steady state earlier than Pz, with one extra cycle compared to Pz. However, considering that this initial cycle may also be influenced by other event-related potentials (ERPs), its formation may be more complex than subsequent cycles.

C. Time-Frequency ERSP and ITPC

We computed ERSP and ITPC separately for each subject and presented the group-averaged results in Fig. 6. Here, we chose CP3 and CP4 for display rather than the traditional C3 and C4 in MI studies, considering that parietal channels exhibited more distinct features under the AORI paradigm, as demonstrated in Section III-A.

The ERSP figure illustrated power decreases in alpha and beta bands during the AORI stage. The decrease in the alpha band was more pronounced. The ITPC figure presented phase-locking of the EEG components at the movement frequency during the AORI stage. It is noteworthy that both ERSP and ITPC demonstrated lateralization.

D. Motor Decoding Results

Fig. 7 and Table I show the four-class SSMRR-based decoding results under the AORI paradigm (A more detailed bar plot displaying the subject-level results can be found in supplementary Fig. 6). The decoding results obtained from each channel selection were far above the theoretical chance level of 25%. The utilization of channels from the motor and visual (referred to as motor-visual in the following text) regions resulted in the highest decoding accuracy at 92.16%±7.61%, which exhibited no significant difference compared to utilizing all three regions and was significantly superior to other results ($p < 0.001$). The decoding results using the motor or visual regions were notably higher than those using the frontal region. Additionally, the inclusion of the frontal region alongside the motor region or visual region only provided limited

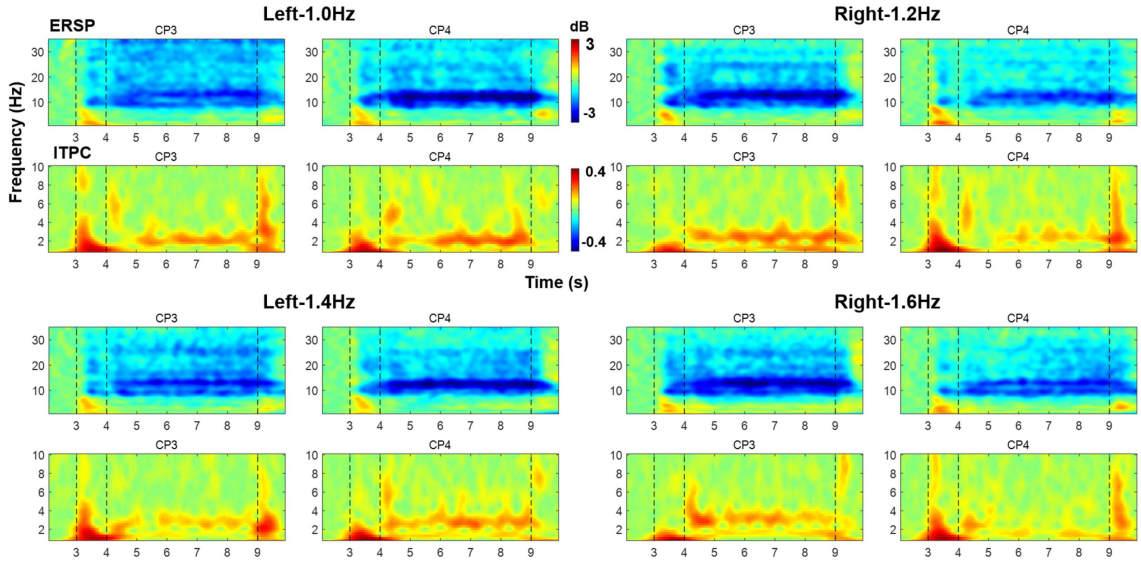

Fig. 6. Group-level ERSP and ITPC. The ERSP illustrated power decreases in alpha and beta bands, and the ITPC presented phase-locking of the EEG components at the movement frequency. Both ERSP and ITPC demonstrated the lateralization.

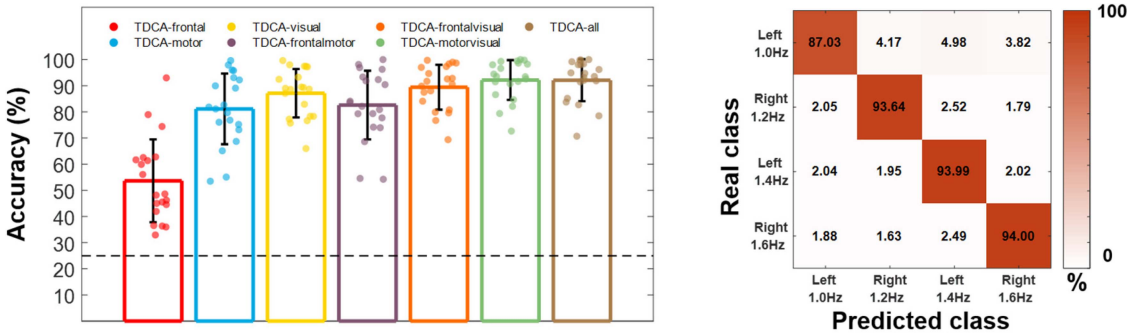

Fig. 7. The four-class SSMRR-based decoding results using channels from different regions. The circular markers represent individual subjects, while the error bars indicate the standard deviation. The horizontal dashed line indicates the theoretical chance level. The confusion matrix demonstrated the results using channels from the motor and visual (referred to as motor-visual) regions.

TABLE I
THE FOUR-CLASS SSMRR-BASED DECODING RESULTS

Region	Frontal	Motor	Visual	Frontal-Motor	Frontal-Visual	Motor-Visual	All-Region
Accuracy (%)	53.64 ± 15.81	81.13±13.51	87.13±9.26	82.59±13.13	89.41±8.58	**92.16±7.61**	92.10±8.03
Motor-Visual	*** $p = 8.86\times10^{-5}$	*** $p = 8.86\times10^{-5}$	*** $p = 8.86\times10^{-5}$	*** $p = 1.32\times10^{-4}$	*** $p = 1.20\times10^{-4}$	\	n.s. $p = 0.9519$

The result obtained from motor-visual region was compared pairwise with those from other regions using wilcoxon signed-rank test ("n.s." indicates not significant, "*" indicates $p < 0.05$, "**" indicates $p < 0.01$, and "***" indicates $p < 0.001$).

improvement in the results. The confusion matrix for the decoding results using motor-visual region is shown in Fig. 7, where the decoding accuracy for the 1.0 Hz-left hand task was slightly lower than the other three tasks, while the accuracies for the other three tasks were roughly the same.

We further examined the relationship between decoding accuracy (motor-visual region) and time window length (Fig. 8). For time windows shorter than 3 seconds, there was a rapid increase in overall accuracy as the window length increased. This increase slowed when the window length surpassed 3 seconds. The distribution of individual results (datapoints in the Fig. 8) also changed with the time window length. As the time window length increased, there was a transition from a few individuals exhibiting exceptionally superior results compared to the majority, to only a few individuals displaying noticeably inferior results. Within a time window of 3 seconds, the majority of subjects have achieved a high level of accuracy (over 80%).

TABLE II
THE BINARY SMR-BASED DECODING RESULTS

Subject	S1	S2	S3	S4	S5	S6	S7	S8	S9	S10	S11	S12	S13	S14	S15	S16	S17	S18	S19	S20	Mean
Acc (%)	64.04	87.63	77.75	73.88	54.29	55.58	96.21	54.38	57.38	70.96	62.46	77.75	64.00	67.96	53.46	67.25	91.88	80.29	93.38	92.79	72.16±14.44
Std (%)	6.45	3.56	4.58	6.11	5.34	6.42	2.82	6.00	6.21	5.03	5.55	4.96	6.16	5.45	6.18	5.71	3.14	4.57	3.15	2.73	

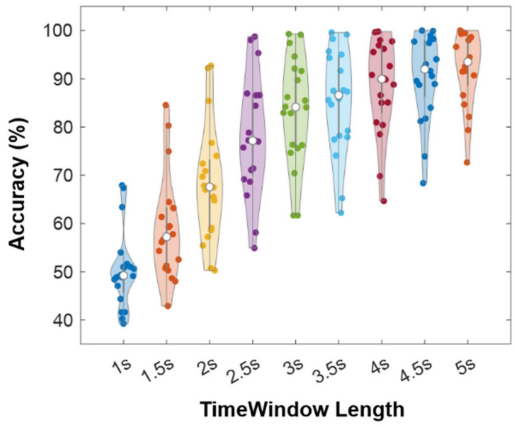

Fig. 8. The four-class SSMRR-based decoding results with different time window lengths (using channels from the motor-visual region).

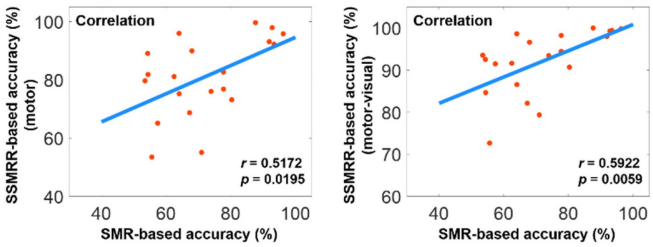

Fig. 9. The correlation between SSMRR-based decoding results and SMR-based decoding results. In the left figure, the SSMRR-based decoding results were obtained from the motor region, while in the right figure, they were obtained from the motor-visual region.

Table II presents the binary SMR-based decoding results. The mean accuracy of 20 subjects was 72.16%±14.44%. Although some subjects exhibited high accuracies above 90% (S7, S17, S19, S20), some subjects only achieved accuracies slightly higher than the theoretical chance level (S5, S6, S8, S9, S15). This result demonstrated noticeable individual differences.

IV. DISCUSSION

In the current study, we proposed the AORI paradigm and presented the AORI-activated brain pattern from multiple perspectives. The distinct pattern was manifested not only as lateralized ERD in the alpha and beta bands but also as a clear spatial distribution of SSMRR at the observed and imagined movement frequencies and their first harmonics. Based on SSMRR, we achieved a promising 92.16%±7.61% accuracy for the four-class decoding task.

A. The Brain Pattern Activated by AORI

The activated spatial pattern highlighted the involvement of a wide range of brain areas, including frontal, sensorimotor, posterior parietal, and occipital regions. Our ERD results were consistent with the findings of Babiloni and colleagues, who reported that the ERD peak was well represented in the posterior parietal and parieto-occipital cortex during action observation but not action execution, especially in the alpha band [46]. Importantly, the AORI paradigm differs from the conventional MI and AO paradigm in that it activates distinct patterns not only in the alpha and beta bands, but also in the movement frequencies and their first harmonics. Our result presented that SSMRR can be induced even without actual movement, thereby expanding upon previous findings [30], [35]. Furthermore, in contrast to previous MI studies that predominantly focused on the sensorimotor region, our results demonstrated the importance of the posterior parietal region in AORI paradigm, as well as the involvement of the frontal region (Fig. 3). This could imply that the AORI task, which simultaneously involves spatial attention, working memory, and mental imagery, activated the dorsal frontoparietal network (dFPN) [47] that supports various cognitive and motor functions. Actually, the dFPN is considered to be the core of motor emulation, defined as establishing a dynamic representation of abstract movement kinematics, sustaining the internal manipulation of this representation, and ensuring its maintenance over short time periods [47].

The observed activated pattern in the occipital region was not reported in previous studies focusing on executed rhythmic movements [30], [35]. This finding is not surprising, given the involvement of visual processes in the AORI task. However, we suggest that these rhythmic components in the occipital region differ from SSVEP for two reasons: 1) It is generally believed that stimulus with frequency higher than 6 Hz can induce SSVEP, while stimulus lower than 2 Hz induces transient VEP [48]. 2) Lateralization was observed at the fundamental frequency, and the spatial pattern differed between the fundamental and harmonic frequencies. These phenomena were not reported in SSVEP studies. In fact, the way of presenting periodicity differs between the AORI and SSVEP paradigms. The AORI paradigm provides rhythmic movement guidance, whereas the SSVEP paradigm presents periodic changes in luminance. In the SSMVEP paradigm, although movement is introduced in the design to make the stimulus presentation more natural, the frequency characteristics induced by SSMVEP focused on the stimulus frequency rather than the movement frequency [14], [22], [28]. In our previous work [30], SSMRR was proposed as a broad term to describe brain activity that exhibits frequency consistency with rhythmic movement. Here, we also consider

TABLE III
THE BINARY SSMRR-BASED DECODING RESULTS (MOTOR-VISUAL REGION)

	Left-1.0Hz /Right-1.2Hz	Left-1.0Hz /Left-1.4Hz	Left-1.0Hz /Right-1.6Hz	Right-1.2Hz /Left-1.4Hz	Right-1.2Hz /Right-1.6Hz	Left-1.4Hz /Right-1.6Hz
Accuracy (%)	94.74±4.86	92.96±7.17	94.33±5.18	95.35±5.47	95.41±4.40	94.45±5.90

this occipital activity observed under the AORI paradigm as SSMRR.

In the results of the time-frequency analysis, we found that although the ITPC at the movement frequency was clear, no evident power increase was observed in the ERSP plots at the movement frequency. We have two possible explanations for this phenomenon, each related to a hypothesis regarding the mechanism underlying SSMRR generation. The first explanation is that SSMRR manifests as a power increase at the movement frequency. However, due to its low frequency, the 1/f background noise may mask these task-related power changes [49]. Compared to ERSP, ITPC is more robust against noise and can still be observed (We conducted a simulation to demonstrate this, which can be seen in supplementary Fig. 7). The second explanation is that SSMRR originates from phase reset [50]. Therefore, it does not cause significant changes in amplitude and power but does lead to phase coupling.

B. The Decoding Performance Under AORI

In this study, we have conducted the SSMRR-based four-class decoding and SMR-based binary decoding. The results demonstrated that from the perspectives of decodable classes, accuracy, and individual differences, SSMRR-based decoding is more effective than SMR-based decoding in the AORI paradigm. The highest decoding accuracy was obtained using channels from the motor-visual region. This result is consistent with the finding that SSMRR was prominently observed in the central, posterior parietal, and occipital regions. Interestingly, we found a significant linear relationship between SSMRR-based and SMR-based decoding results. This indicated that although SSMRR and SMR are different features, they may consistently reflect the effectiveness of the subjects' motor imagery.

In this study, the experiment task incorporated left- and right-hand design in addition to the four frequency conditions. There are two primary reasons. First, we aimed to investigate whether a lateralized brain pattern could be activated by left- or right- hand related AORI tasks. Second, TDCA, as a spatial filtering method, may also utilize spatial features beyond the temporal periodic features. Nevertheless, the binary decoding results (Table III) demonstrated that temporal periodic features of SSMRR at different frequencies are more dominant than spatial features. The decoding accuracy for different frequencies within the same task hand is similar to the accuracy when both the task hand and frequency differ. This indicated that the temporal periodic features alone have maintained a relatively high level of accuracy, with minimal additional contribution from spatial information.

Although a cross-study comparison of decoding accuracy is not entirely rigorous, we believe that achieving an accuracy of 92.16% ± 7.61% for four-class motor decoding is an encouraging result. Specifically, this result outperformed most SMR-based decoding reported in existing studies. We suggest that the temporal periodic SSMRR features are more robust and consistent across trials and subjects than conventional SMR features. Moreover, SMR-based decoding typically employs CSP-based algorithms to leverage spatial features. In contrast, SSMRR-based decoding relies on TDCA or TRCA to efficiently utilize temporal periodic features, thereby taking full advantage of the high signal-to-noise ratio (SNR) of periodic signals [40], [51], [52].

Our decoding results also indicated that, using the AORI paradigm and TDCA method, movements with frequency differences as small as 0.2 Hz can be accurately classified. The movement frequency range was 1.0 Hz to 1.6 Hz in the current study. Building on this, we introduced four additional tasks (1.8 Hz-left, 2.0 Hz-right, 2.2 Hz-left, 2.4 Hz-right) and conducted a preliminary attempt at 8-class decoding (included 6 subjects), achieving an average accuracy of 89.20% ± 7.67% (please refer to the supplementary materials for detailed information). This suggested that the frequency range in the current study could be further broadened, thereby allowing for an expansion in the number of decodable classes.

C. Possible Variants and Applications of AORI

The AORI paradigm can serve as the foundation for designing natural and robust closed-loop BCI. In the AORI paradigm, features are derived from the rhythms of AO-guided imagination, without the need for additional high-frequency stimuli. The high decoding accuracy of different movement frequencies makes brain-actuating an exoskeleton at different speeds possible. We would like to clarify that the movement type in the AORI paradigm can vary and is not limited to hand movements. Consider a scenario for upper limb rehabilitation where the user imagined a 1.5 Hz rhythm, and the brain-controlled upper limb exoskeleton would move at the same frequency. This intuitive mapping between intention and feedback can enhance the sense of agency [31], [32].

The AORI paradigm can also be further developed to study cognitive processes such as neural entrainment. Neural entrainment is the phenomenon that neural oscillations can follow the rhythms of dynamic sensory stimuli [53], [54]. It is an important topic in the field of neuroscience since it involves the interaction of the brain and the environment. Traditionally, experimental methods used for studying neural entrainment include rhythmic visual rotation [55], rhythmic metronome, and finger tapping [56]. Our results demonstrated that humans can voluntarily modulate their mental activity to synchronize with a specific rhythm. Therefore, AORI can serve as a supplement to the aforementioned experimental methods.

D. Limitations and Future Work

The findings in the current study have shown the electrophysiological features induced by the AORI paradigm. However, some interesting phenomena still lack investigation into their underlying mechanisms. Firstly, as we have mentioned in Section IV-A, whether SSMRR is additive to the ongoing background or resetting of ongoing background remains unclear. Actually, the same question also puzzled researchers in ERP field [57] and is still open. Secondly, further experiments could be designed to investigate the phase characteristics under the AORI task. The time series demonstrated that certain channels (e.g., P9, P10, Oz) exhibited an additional cycle at the onset of the AORI stage compared to other channels. With the current experiment design, the interference from ERP makes it hard to ascertain whether this initial cycle of the periodic signal represents SSMRR. This uncertainty affects the assessment of absolute phase differences between channels. Recently, the concept of traveling waves has attracted significant attention [58], [59]. The timing and direction of traveling waves reflect the interactions between different brain regions during various cognitive and behavioral processes [59], [60]. Therefore, further investigation of phase characteristics under the AORI paradigm could explore how information is transmitted between brain regions, thereby providing insights into how the brain processes rhythm.

In the context of BCI applications, we have demonstrated the potential of AORI in high-performance multiclass motor decoding. Future efforts will focus on transitioning AORI from offline to online, from synchronous to asynchronous, and from healthy individuals to those with motor disorders. Ultimately, the goal is to make AORI-BCI an effective tool for motor learning, motor control, and motor rehabilitation.

V. Conclusion

We proposed a novel BCI paradigm named AORI, which is easily comprehensible and design-friendly. From a frequency perspective, AORI can not only induce ERD in the alpha and beta bands but also induce SSMRR, which is the rhythmic activity at the movement frequency and its first harmonic. From a spatial pattern perspective, AORI involves the participation of multiple brain areas, including the frontal, sensorimotor, posterior parietal, and occipital regions, with a clear lateralization. In terms of decoding, we achieved high performance ($92.16\% \pm 7.61\%$) in four-class motor decoding using the AORI paradigm. Overall, our findings provide new possibilities for designing a natural and robust BCI for motor control and motor rehabilitation.

References

[1] J. R. Wolpaw et al., "Brain–computer interfaces for communication and control," *Clin. Neurophysiol.*, vol. 113, no. 6, pp. 767–791, Jun. 2002, doi: 10.1016/S1388-2457(02)00057-3.

[2] B. He et al., "Brain–computer interfaces," in *Neural Engineering*, B. He, Ed. Cham, Switzerland: Springer, 2020, pp. 131–183.

[3] H. Yuan and B. He, "Brain–computer interfaces using sensorimotor rhythms: Current state and future perspectives," *IEEE Trans. Biomed. Eng.*, vol. 61, no. 5, pp. 1425–1435, May 2014, doi: 10.1109/tbme.2014.2312397.

[4] R. Mane et al., "BCI for stroke rehabilitation: Motor and beyond," *J. Neural Eng.*, vol. 17, no. 4, Aug. 2020, Art. no. 041001, doi: 10.1088/1741-2552/aba162.

[5] K. LaFleur et al., "Quadcopter control in three-dimensional space using a noninvasive motor imagery-based brain–computer interface," *J. Neural Eng.*, vol. 10, no. 4, Jun. 2013, Art. no. 046003, doi: 10.1088/1741-2560/10/4/046003.

[6] B. J. Edelman et al., "Noninvasive neuroimaging enhances continuous neural tracking for robotic device control," *Sci. Robot.*, vol. 4, no. 31, 2019, Art. no. eaaw6844, doi: 10.1126/scirobotics.aaw6844.

[7] L. Tonin, F. C. Bauer, and J. del Millán, "The role of the control framework for continuous teleoperation of a brain–machine interface-driven mobile robot," *IEEE Trans. Robot.*, vol. 36, no. 1, pp. 78–91, Feb. 2020, doi: 10.1109/TRO.2019.2943072.

[8] F. Pichiorri et al., "Brain–computer interface boosts motor imagery practice during stroke recovery," *Ann. Neurol*, vol. 77, no. 5, pp. 851–865, 2015, doi: 10.1002/ana.24390.

[9] R. Foong et al., "Assessment of the efficacy of EEG-based MI-BCI with visual feedback and EEG correlates of mental fatigue for upper-limb stroke rehabilitation," *IEEE Trans. Biomed. Eng.*, vol. 67, no. 3, pp. 786–795, Mar. 2020, doi: 10.1109/tbme.2019.2921198.

[10] A. Vuckovic and B. A. Osuagwu, "Using a motor imagery questionnaire to estimate the performance of a brain–computer Interface based on object oriented motor imagery," *Clin. Neurophysiol.*, vol. 124, no. 8, pp. 1586–1595, 2013, doi: 10.1016/j.clinph.2013.02.016.

[11] D. L. Eaves et al., "Motor imagery during action observation: A brief review of evidence, theory and future research opportunities," *Front. Neurosci.*, vol. 10, 2016, Art. no. 23652, doi: 10.3389/fnins.2016.00514.

[12] L. Zhang et al., "Enhancing visual-guided motor imagery performance via sensory threshold somatosensory electrical stimulation training," *IEEE Trans. Biomed. Eng.*, vol. 70, no. 2, pp. 756–765, Feb. 2023, doi: 10.1109/tbme.2022.3202189.

[13] M. Ahn and S. C. Jun, "Performance variation in motor imagery brain–computer interface: A brief review," *J. Neurosci. Methods*, vol. 243, pp. 103–110, 2015, doi: 10.1016/j.jneumeth.2015.01.033.

[14] X. Zhang et al., "Can a highly accurate multi-class SSMVEP BCI induce sensory-motor rhythm in the sensorimotor area?," *J. Neural Eng.*, vol. 18, no. 3, 2021, Art. no. 2684, doi: 10.1088/1741-2552/ab85b2.

[15] S. Vogt et al., "Multiple roles of motor imagery during action observation," *Front Hum. Neurosci.*, vol. 7, 2013, Art. no. 807, doi: 10.3389/fnhum.2013.00807.

[16] D. Ertelt et al., "Action observation has a positive impact on rehabilitation of motor deficits after stroke," *NeuroImage*, vol. 36, pp. T164–T173, 2007, doi: 10.1016/j.neuroimage.2007.03.043.

[17] T. Mulder, "Motor imagery and action observation: Cognitive tools for rehabilitation," *J. Neural Transmiss.*, vol. 114, no. 10, pp. 1265–1278, 2007, doi: 10.1007/s00702-007-0763-z.

[18] G. Buccino, "Action observation treatment: A novel tool in neurorehabilitation," *Philos. Trans. Roy. Soc. B: Biol. Sci.*, vol. 369, 2014, Art. no. 1644, doi: 10.1098/rstb.2013.0185.

[19] H. Nagai and T. Tanaka, "Action observation of own hand movement enhances event-related desynchronization," *IEEE Trans. Neural Syst. Rehabil. Eng.*, vol. 27, no. 7, pp. 1407–1415, Jul. 2019, doi: 10.1109/tnsre.2019.2919194.

[20] H. Yokoyama et al., "Neural decoding of gait phases during motor imagery and improvement of the decoding accuracy by concurrent action observation," *J. Neural Eng.*, vol. 18, no. 4, 2021, Art. no. 2652, doi: 10.1088/1741-2552/ac07bd.

[21] N. Rungsirisilp et al., "Applying action observation during a brain-computer interface on upper limb recovery in chronic stroke patients," *IEEE Access*, vol. 11, pp. 4931–4943, 2023, doi: 10.1109/access.2023.3236182.

[22] X. Zhang et al., "A novel online action observation-based brain–computer interface that enhances event-related desynchronization," *IEEE Trans. Neural Syst. Rehabil. Eng.*, vol. 29, pp. 2605–2614, 2021, doi: 10.1109/tnsre.2021.3133853.

[23] M. G. Kim et al., "Brain–Computer interface-based action observation combined with peripheral electrical stimulation enhances corticospinal excitability in healthy subjects and stroke patients," *J. Neural Eng.*, vol. 19, no. 3, 2022, Art. no. 35675795, doi: 10.1088/1741-2552/ac76e0.

[24] R. Zhang et al., "Hybrid brain-computer interface controlled soft robotic glove for stroke rehabilitation," *IEEE J. Biomed. Health Inform.*, vol. 28, no. 7, pp. 4194–4203, Jul. 2024, doi: 10.1109/jbhi.2024.3392412.

[25] A. Ravi et al., "Enhanced system robustness of asynchronous BCI in augmented reality using steady-state motion visual evoked potential," *IEEE Trans. Neural Syst. Rehabil. Eng.*, vol. 30, pp. 85–95, 2022, doi: 10.1109/tnsre.2022.3140772.
[26] D. Hu et al., "Steady-state motion visual evoked potential (SSMVEP) based on equal luminance colored enhancement," *PLoS One*, vol. 12, no. 1, 2017, Art. no. 2362, doi: 10.1371/journal.pone.0169642.
[27] W. Yan et al., "Four novel motion paradigms based on steady-state motion visual evoked potential," *IEEE Trans. Biomed. Eng.*, vol. 65, no. 8, pp. 1696–1704, Aug. 2018, doi: 10.1109/tbme.2017.2762690.
[28] X. Zhang et al., "Performance of the action observation-based brain–computer interface in stroke patients and gaze metrics analysis," *IEEE Trans. Neural Syst. Rehabil. Eng.*, vol. 32, pp. 1370–1379, 2024, doi: 10.1109/tnsre.2024.3379995.
[29] J. Xie et al., "Effects of mental load and fatigue on steady-state evoked potential based brain computer interface tasks: A comparison of periodic flickering and motion-reversal based visual attention," *PLoS One*, vol. 11, no. 9, 2016, Art. no. e0163426, doi: 10.1371/journal.pone.0163426.
[30] Y. Wei et al., "Decoding movement frequencies and limbs based on steady-state movement-related rhythms from noninvasive EEG," *J. Neural Eng.*, vol. 20, no. 6, Nov. 2023, Art. no. 066019, doi: 10.1088/1741-2552/ad01de.
[31] W. Wen and H. Imamizu, "The sense of agency in perception, behaviour and human–machine interactions," *Nat. Rev. Psychol.*, vol. 1, no. 4, pp. 211–222, 2022, doi: 10.1038/s44159-022-00030-6.
[32] A. Serino et al., "Sense of agency for intracortical brain–machine interfaces," *Nat. Hum. Behav.*, vol. 6, no. 4, pp. 565–578, 2022, doi: 10.1038/s41562-021-01233-2.
[33] K. Jerbi et al., "Coherent neural representation of hand speed in humans revealed by MEG imaging," *Proc Natl. Acad. Sci. USA*, vol. 104, no. 18, pp. 7676–7681, 2007, doi: 10.1073/pnas.0609632104.
[34] M. Bourguignon et al., "Neuronal network coherent with hand kinematics during fast repetitive hand movements," *NeuroImage*, vol. 59, no. 2, pp. 1684–1691, Jan. 2012, doi: 10.1016/j.neuroimage.2011.09.022.
[35] M. Bourguignon et al., "Coupling between human brain activity and body movements: Insights from non-invasive electromagnetic recordings," *NeuroImage*, vol. 203, Dec. 2019, Art. no. 116177, doi: 10.1016/j.neuroimage.2019.116177.
[36] A. Osman et al., "The beat goes on: Rhythmic modulation of cortical potentials by imagined tapping," *J. Exp. Psychol.: Hum. Percep.*, vol. 32, no. 4, pp. 986–1005, Aug. 2006, doi: 10.1037/0096-1523.32.4.986.
[37] A. Kai Keng et al., "Filter bank common spatial pattern (FBCSP) in brain-computer interface," in *Proc. IEEE 2008 Int. Joint Conf. Neural Netw.*, Jun. 2008, pp. 2390–2397, doi: 10.1109/IJCNN.2008.4634130.
[38] Y. Pei et al., "A tensor-based frequency features combination method for brain–computer interfaces," *IEEE Trans. Neural Syst. Rehabil. Eng.*, vol. 30, pp. 465–475, 2022, doi: 10.1109/tnsre.2021.3125386.
[39] H. Fang et al., "Feature extraction method based on filter banks and riemannian tangent space in motor-imagery BCI," *IEEE J. Biomed. Health Inf.*, vol. 26, no. 6, pp. 2504–2514, Jun. 2022, doi: 10.1109/jbhi.2022.3146274.
[40] B. Liu et al., "Improving the performance of individually calibrated SSVEP-BCI by task- discriminant component analysis," *IEEE Trans. Neural Syst. Rehabil. Eng.*, vol. 29, pp. 1998–2007, 2021, doi: 10.1109/TNSRE.2021.3114340.
[41] M. Nakanishi et al., "Enhancing detection of SSVEPs for a high-speed brain speller using task-related component analysis," *IEEE Trans. Biomed. Eng.*, vol. 65, no. 1, pp. 104–112, Jan. 2018, doi: 10.1109/TBME.2017.2694818.
[42] G. Schalk et al., "BCI2000: A general-purpose brain-computer interface (BCI) system," *IEEE Trans. Biomed. Eng.*, vol. 51, no. 6, pp. 1034–1043, Jun. 2004, doi: 10.1109/TBME.2004.827072.
[43] A. Delorme and S. Makeig, "EEGLAB: An open source toolbox for analysis of single-trial EEG dynamics including independent component analysis," *J. Neurosci. Methods*, vol. 134, no. 1, pp. 9–21, Mar. 2004, doi: 10.1016/j.jneumeth.2003.10.009.
[44] C. Y. Chang et al., "Evaluation of artifact subspace reconstruction for automatic artifact components removal in multi-channel EEG recordings," *IEEE Trans. Biomed. Eng.*, vol. 67, no. 4, pp. 1114–1121, Apr. 2020, doi: 10.1109/TBME.2019.2930186.
[45] A. M. Amjad et al., "An extended difference of coherence test for comparing and combining several independent coherence estimates: Theory and application to the study of motor units and physiological tremor," *J. Neurosci. Methods*, vol. 73, no. 1, pp. 69–79, Apr. 1997, doi: 10.1016/S0165-0270(96)02214-5.
[46] C. Babiloni et al., "Human cortical electroencephalography (EEG) rhythms during the observation of simple aimless movements: A high-resolution EEG study," *NeuroImage*, vol. 17, no. 2, pp. 559–572, 2002, doi: 10.1006/nimg.2002.1192.
[47] R. Ptak et al., "The dorsal frontoparietal network: A core system for emulated action," *Trends Cogn. Sci.*, vol. 21, no. 8, pp. 589–599, 2017, doi: 10.1016/j.tics.2017.05.002.
[48] X. Gao et al., "A BCI-based environmental controller for the motion-disabled," *IEEE Trans. Neural Syst. Rehabil. Eng.*, vol. 11, no. 2, pp. 137–140, Jun. 2003, doi: 10.1109/TNSRE.2003.814449.
[49] T. Donoghue et al., "Parameterizing neural power spectra into periodic and aperiodic components," *Nat. Neurosci.*, vol. 23, no. 12, pp. 1655–1665, Dec. 2020, doi: 10.1038/s41593-020-00744-x.
[50] C. C. Canavier, "Phase-resetting as a tool of information transmission," *Curr. Opin. Neurobiol.*, vol. 31, pp. 206–213, Apr. 2015, doi: 10.1016/j.conb.2014.12.003.
[51] J. Jin et al., "Robust similarity measurement based on a novel time filter for SSVEPs detection," *IEEE Trans. Neural Netw. Learn. Syst.*, vol. 34, no. 8, pp. 4096–4105, Aug. 2023, doi: 10.1109/TNNLS.2021.3118468.
[52] C. M. Wong et al., "Spatial filtering in SSVEP-based BCIs: Unified framework and new improvements," *IEEE Trans. Biomed. Eng.*, vol. 67, no. 11, pp. 3057–3072, Nov. 2020, doi: 10.1109/TBME.2020.2975552.
[53] H. Zhou et al., "Interpretations of frequency domain analyses of neural entrainment: Periodicity, fundamental frequency, and harmonics," *Front Hum. Neurosci.*, vol. 10, 2016, Art. no. 25625, doi: 10.3389/fnhum.2016.00274.
[54] P. Lakatos et al., "A new unifying account of the roles of neuronal entrainment," *Curr. Biol.*, vol. 29, no. 18, pp. R890–R905, Sep. 2019, doi: 10.1016/j.cub.2019.07.075.
[55] P. Albouy et al., "Supramodality of neural entrainment: Rhythmic visual stimulation causally enhances auditory working memory performance," *Sci. Adv.*, vol. 8, no. 8, 2022, Art. no. eabj9782, doi: 10.1126/sciadv.abj9782.
[56] M. Rosso et al., "Neural entrainment underpins sensorimotor synchronization to dynamic rhythmic stimuli," *NeuroImage*, vol. 277, 2023, Art. no. 120226, doi: 10.1016/j.neuroimage.2023.120226.
[57] P. Sauseng et al., "Are event-related potential components generated by phase resetting of brain oscillations? A critical discussion," *Neuroscience*, vol. 146, no. 4, pp. 1435–1444, Jun. 2007, doi: 10.1016/j.neuroscience.2007.03.014.
[58] A. Alamia and R. VanRullen, "Alpha oscillations and traveling waves: Signatures of predictive coding?," *PLoS Biol.*, vol. 17, no. 10, Oct. 2019, Art. no. e3000487, doi: 10.1371/journal.pbio.3000487.
[59] U. R. Mohan et al., "The direction of theta and alpha travelling waves modulates human memory processing," *Nat. Hum. Behav.*, vol. 8, pp. 1124–1135, Mar. 2024, doi: 10.1038/s41562-024-01838-3.
[60] D. R. Belov et al., "Traveling waves in the human EEG during voluntary hand movements," *Neurosci. Behav. Physiol.*, vol. 45, no. 9, pp. 1043–1054, 2015, doi: 10.1007/s11055-015-0184-7.